Study of electrical properties of nickel doped SnO$_2$ ceramic nanoparticles

Ameer Azam*, Arham S. Ahmed, M. Shahnawaze Ansari, Muhamed Shafeeq M, Alim H. Naqvi

Centre of Excellence in Materials Science (Nanomaterials), Department of Applied Physics, Z. H. College of Engineering & Technology, Aligarh Muslim University, Aligarh 202002, U.P., India

ARTICLE INFO

ABSTRACT

Nickel doped tin oxide (Sn$_{1-x}$Ni$_x$O$_2$, where x = 0, 0.05, 0.07 and 0.09) nanoparticles with sub-5 nm size were synthesized using sol–gel method. The structural and compositional analyses were carried out using XRD, FESEM and EDAX. Electrical properties were studied using dielectric and impedance spectroscopy at room temperature. XRD analysis indicated the formation of single phase rutile structure of all the samples. The particle size was observed to vary from 5 nm to 2 nm as the nickel content was increased. The XRD and EDAX results corroborated the successful doping of Ni in the SnO$_2$ matrix. The dielectric constant ε', ε'', loss tangent tan δ and ac conductivity σ_{ac} were studied as a function of frequency and composition and the behaviour has been explained on the basis of Maxwell–Wagner model. Complex impedance analysis which was used to separate the grain and grain boundary contributions to the system suggests the dominance of grain boundary resistance in the doped samples.

1. Introduction

Nanomaterials are highly sensitive and functionally efficient because of smaller grain size and high surface to volume ratio as compared to the conventional materials in micrometer range. Nanocrystalline metal oxides have drawn a great deal of attention due to their excellent properties arising out of large surface area, high sinterability, quantum confinement effect, etc. which are dependent on the shape and size of the crystal. Tin oxide (SnO$_2$) is one of the most important n-type metal oxide semiconductors with wide band gap (3.6 eV at 300 K) [1]. Because of its unique electronic, optical, electrochemical and catalytic properties, it has been widely used in flat panel displays, transparent conducting electrodes, solar cells, gas sensors and rechargeable Li-ion batteries, etc. [2]. The interest in SnO$_2$ is evinced because it is a naturally non-stoichiometry prototype transparent conducting oxide (TCO) having high transparency in visible region and high reflectivity in IR region. Further, the electrical resistance of SnO$_2$ is small [3]. Electrical conduction in transparent solids occurs in just a few systems such as 4d metal oxides SnO$_2$ and In$_2$O$_3$. However, the reason for this coexistence of electrical conductivity with optical transparency is yet to be explained clearly. Nevertheless, it has been postulated that the transparent conductivity is related to the existence of shallow donor levels near the conduction band formed by large concentration of oxygen vacancies [4]. It is generally observed that increasing the surface/bulk or surface to volume ratio by decreasing the grain size of rutile SnO$_2$ nanoparticles is crucial for achieving high sensitivity in gas sensors [5]. One of the most important methods to modify the characteristics of the materials is the introduction of dopants in the parent system. It has been shown that several dopants (Cr, Co, Mn, Al, Mg, Cu, Fe) can lead to an increase of surface area of SnO$_2$ powder [5]. These dopants stabilize the surface and promote a reduction in size. To get the optimum advantage of the properties of metal ions doped SnO$_2$ nanoparticles, a number of methods have been developed for the effective synthesis of metal doped SnO$_2$ nanoparticles. Some of them are mechanical alloying [6], CVD [7], sol–gel method [8], solvothermal method [9], spray pyrolysis [10], gel combustion method [11], physical vapor deposition [12], etc. In the present work, we have synthesized Ni-doped SnO$_2$ nanoparticles (Sn$_{1-x}$Ni$_x$O$_2$, where x = 0, 0.05, 0.07 and 0.09) using sol–gel method. This method has some advantages such as low temperature synthesis, precise control over stoichiometry and high purity.

Electrical properties of tin oxide are of great importance from the technological point of view. Tin oxide is a wide band gap semiconductor which in its stoichiometric form shows insulating behaviour. Non-stoichiometry, particularly oxygen vacancies, makes it conducting. The formation energy of oxygen vacancies and tin interstitials in SnO$_2$ is very low and thus these defects form readily, resulting in the observed high conductivity of non-stoichiometric SnO$_2$ [4]. Electrical properties such as charge carrier concentration and conductivity can further be improved by extrinsic dopants. Usually Sb as a cation and F as an anion have been reported to improve the conductivity of SnO$_2$ [13].

* Corresponding author. Tel.: +91 9319788742; fax: +91 5712700042.
E-mail addresses: azam222@rediffmail.com, ameerazam2009@gmail.com (A. Azam).

There are many papers reported in the literature that emphasize the gas sensing properties of pure and doped tin oxide ceramics, e.g. Tan et al. reported the gas sensing properties of nanostructured SnO_2 [14]; Jain et al. reported the effect of Ni doping on SnO_2 gas sensors [15]. However, there are only very few number of papers that focus on the electrical properties of SnO_2. Aguiler Martinez et al. reported the microstructure and electrical properties of SnO_2 doped with Co, Sb, and Na [16]. Yadav et al. studied electrical, structural and optical properties of SnO_2:F thin films and reported that at lower substrate temperature amorphous films are formed while at higher temperatures ($T > 450\,^\circ$C), crystalline SnO_2:F films with preferential growth along (2 0 0) plane have been observed. The films deposited at $475\,^\circ$C substrate temperature were found to have relatively lower resistivity of $3.91 \times 10^{-4}\,\Omega$ cm [17]. Joseph et al. discussed electrical and optical properties of Cu, Fe, Mn doped SnO_2 films [18], they have shown that the conductivity enhances remarkably on Fe (2 and 3 wt%) and Cu (2 wt%) doping. It may be noticed that little work is reported on the detailed dielectric and impedance behaviour of SnO_2. Further, compared to optoelectronic properties, the dielectric behaviour of SnO_2 nanoparticles is also poorly known. Gaponov and Glot have studied the electrical properties of SnO_2 based ceramics with CuO addition, and have reported the decrease in relative dielectric constant with higher concentration of CuO [19]. Li et al. have reported the synthesis, photoluminescence and dielectric properties of O-deficient SnO_2 nanowires in which they have shown that the relative dielectric constant of SnO_2 nanowires enhanced compared to the bulk [1]. We understand that the study of electrical properties of Ni-doped SnO_2 ceramic nanoparticles is a least explored area till now and we have, therefore, been motivated to take up this task. In this paper, we are reporting structural and electrical properties such as dielectric constant (ε), tangent loss ($\tan\delta$), ac conductivity (σ_{ac}), real and imaginary part of impedance and Cole–Cole analysis of pure and Ni-doped SnO_2 using XRD, SEM, dielectric and impedance spectroscopy.
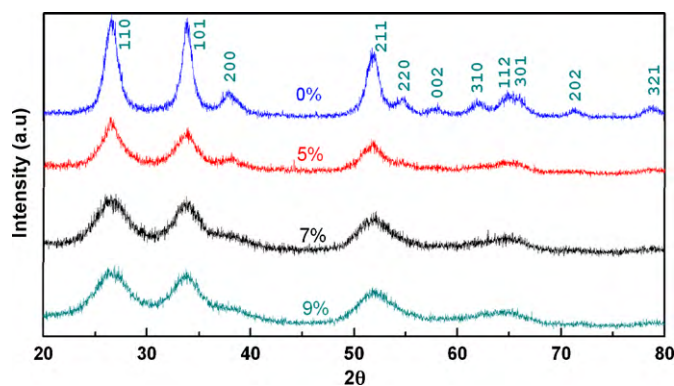
2. Experimental

Analytical grade $SnCl_4 \cdot 5H_2O$ and $NiCl_2 \cdot 2H_2O$ have been used as starting materials for the synthesis of $Sn_{1-x}Ni_xO_2$ series. In the present synthesis procedure, citric acid was added to 50 ml of distilled water with magnetic stirring, until pH became 1.5. Then the required amounts of $SnCl_4 \cdot 5H_2O$ and $NiCl_2 \cdot 2H_2O$ with ($x = 0, 0.05, 0.07$ and 0.09) were added and dissolved. This was followed by the addition of 10 ml of ethylene glycol to the above solution which was then stirred for 20 min. Later, sufficient amount of aqueous ammonia (15 mol/L) was added drop wise to the above solution under magnetic stirring for 30 min. Finally, a light greenish gel was obtained, which was washed with water and alcohol several times, and was dried at $120\,^\circ$C for 15 h in an oven. The dried gel powder was further calcined at $350\,^\circ$C for 2 h resulting in the formation of Ni-doped SnO_2 nanoparticles. The SnO_2 nanopowder thus obtained was pressed into pellets of 13 mm diameter and 1 mm thickness, which were further sintered at $1000\,^\circ$C for 6 h. Crystallinity, structure and particle size of Ni-doped SnO_2 nanoparticles were determined by X-ray diffraction (XRD) using Cu-Kα radiations ($\lambda = 0.15406$ nm) in 2θ range from 20° to 80° with scan rate of 2°/min. Morphological analysis was carried out on a FEI FESEM. The compositional analysis was carried out using EDAX attached with the FESEM. Dielectric and impedance spectroscopy measurements were carried out in the frequency range 42 Hz to 5 MHz using LCR HI-Tester (HIOKI 3532-50). The pellets were coated on adjacent faces with silver paste, thereby forming parallel plate capacitor geometry.

The value of dielectric constant (ε') is calculated using the formula:

$$\varepsilon' = \frac{C_p \times d}{\varepsilon_0 A}$$

Fig. 1. XRD patterns of Ni-doped SnO_2 nanoparticles.

where ε_0 is the permittivity of free space, d is thickness of pellet, A is the cross-sectional area of the flat surface of the pellet and C_p is the capacitance of the specimen in Farad (F).

The complex dielectric constant ε'' of the samples was calculated using the relation:

$$\varepsilon'' = \varepsilon' \tan\delta$$

where $\tan\delta$ is the dielectric loss tangent which is proportional to the loss of energy from the applied field into the sample (this energy is dissipated as heat) and therefore denoted as dielectric loss.

The ac conductivity of the samples was determined using the relation:

$$\sigma_{ac} = \varepsilon' \varepsilon_0 \omega \tan\delta$$

where ω is the angular frequency.

3. Results and discussion

3.1. Structural properties

The typical XRD patterns of the pure and Ni-doped SnO_2 samples annealed at $350\,^\circ$C are shown in Fig. 1. The peak positions of each sample exhibit the rutile structure of SnO_2 which were confirmed from the ICDD card No. 77-0452. Further, no other impurity peak was observed in the XRD pattern showing the single phase sample formation. The crystalline size was calculated using Scherrer formula, $D = 0.9\lambda/(\beta\cos\theta)$ [20], where λ is the wavelength of X-ray radiation, β is the full width at half maximum (FWHM) of the peaks at the diffracting angle θ. The calculated particle sizes of each sample are depicted in Table 1. It can be observed from Table 1 that the crystalline size of SnO_2 decreased from 5 nm to 2 nm when Ni^{2+} content increased from 0% to 9%. The data revealed that the presence of Ni^{2+} ions in SnO_2 prevented the growth of crystal grains. The variations in the lattice parameters and cell volume have also been studied for different doping concentrations and presented in Table 1. The ionic radius of Ni^{2+} is 69 pm whereas that of Sn^{4+} is 71 pm. The Ni ions substitute the Sn^{4+} ions in the crystal due to comparable ionic radius. However, the decrease in the lattice parameter may be due to the smaller ionic radius of Ni ions. The XRD spectra have also been used to study the crystallinity of the samples. The doping of nickel in SnO_2 not only lowers the particle size but also degrades the crystallinity of the nanoparticles. Similar results have been reported earlier by various authors [21–23].
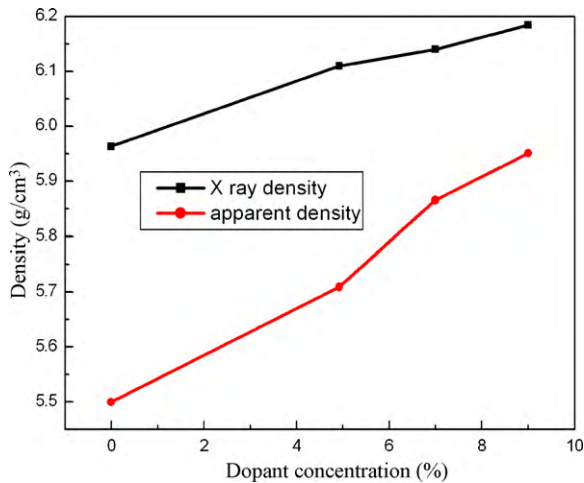
Table 1
Variation of crystallite size, lattice parameters and cell volume with doping.

Dopant concentration (%)	Crystallite size (nm)	Lattice parameter, a (Å)	Lattice parameter, c (Å)	Cell volume (Å³)
0	5.0	4.803	3.205	73.93
5	3.8	4.799	3.201	73.72
7	2.6	4.791	3.195	73.33
9	2.0	4.781	3.189	73.13

Fig. 2. Variation of X-ray density and apparent density with dopant concentration.

As the Ni content increases, the intensity of XRD peaks decreases and FWHM increases (Fig. 1) which shows the degradation of crystallinity. This means that even though the Ni ions occupy the regular lattice site of Sn^{4+}, they produce crystal defects around the dopants and the charge imbalance arisen from these defects changes the stoichiometry of the materials.

Fig. 2 shows the variation of X-ray density (theoretical) and apparent density (observed) with dopant concentration, which were calculated using the relations:

$$D_{hkl} = \frac{ZM}{NV}$$

$$D = \frac{m}{V} = \frac{m}{\pi r^2 h}$$

where D_{hkl} is X-ray density, Z is no. of atoms per unit cell, M is molecular weight of the sample, N is the Avogadro's number, D is apparent density while m, V, r and h are the mass, volume, radius and thickness of the sample respectively. It is clear from Fig. 2 that X-ray density and apparent density both increase with the increase in nickel concentration. It may be due to the fact that density of nickel ions (8.902 g/cm^3) is greater than that of tin ions (7.31 g/cm^3). Moreover, Ni^{2+} is the acceptor dopant for SnO_2 and is usually ionically compensated by the formation of oxygen vacancies. It has also been reported in the literature that the dopants with valence +2 can promote densification of SnO_2 ceramics due to the formation of solid solution with the creation of oxygen vacancies [24]. Cerri et al. have also reported the densification of Co^{2+} and Mn^{2+} doped SnO_2 due to the formation of oxygen vacancies [25]. It is also clear from Fig. 2 that the X-ray density is higher than that of apparent density. It may be due to the existence of pores in the material which depends on the sintering conditions [26].

Fig. 3 shows the typical morphology and composition of pure (Fig. 3a) and 5% Ni-doped (Fig. 3b) SnO_2 nanopowder. Samples were in the powder form for SEM analysis. Powder was stick on the sample holder using double sided tape and gold coated with sputter coater. SEM micrographs show the presence of large spherical aggregates of smaller individual nanoparticles and the presence of Ni is confirmed from the selective area EDAX analysis. It can be verified from the results of XRD and EDAX that the Ni is successfully doped in the SnO_2 nanocrystals. Fig. 4 shows the microstructure of sintered pellet of 5% Ni-doped SnO_2. Fig. 4 clearly depicts the development of grain boundaries in the Ni-doped SnO_2. It may be due to the increase in density and reduction in grain size with doping.

3.2. Dielectric properties

The dielectric constant is represented by $\varepsilon = \varepsilon' - i\varepsilon''$ where ε' is real part of dielectric constant and describes the stored energy
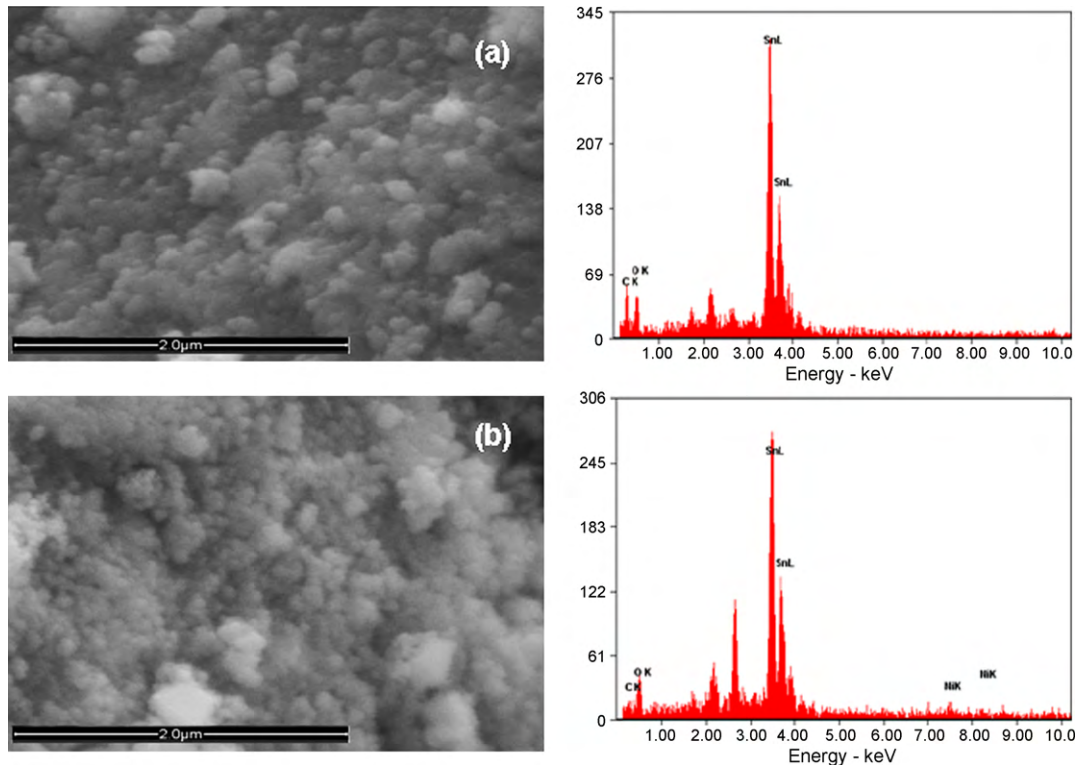

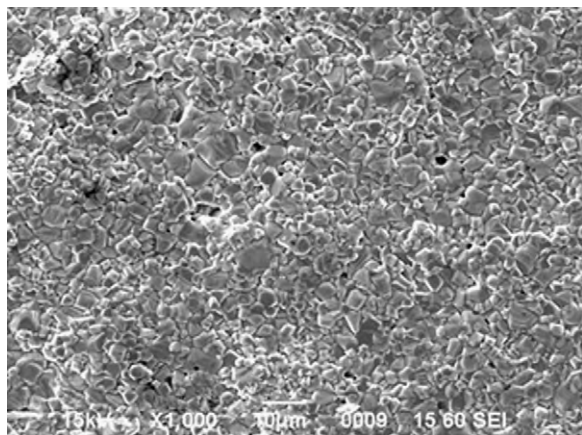**Fig. 3.** SEM and EDAX images of (a) 0% and (b) 5% Ni-doped SnO_2 nanopowder.

Fig. 4. Microstructure of sintered pellet of 5% Ni-doped SnO_2.

Fig. 6. Variation of dielectric loss with frequency.

while ε'' is imaginary part of dielectric constant, which describes the dissipated energy. The dielectric constant as a function of frequency for all compositions is shown in Fig. 5. It is clear from the figure that it has strong frequency dependence in the lower frequency region. The dielectric constant decreases with the increase in frequency and become constant at high frequencies for all compositions and this type of behaviour can be explained on the basis of Maxwell–Wagner model [27]. According to this model, a dielectric medium is assumed to be made of well conducting grains which are separated by poorly conducting (or resistive) grain boundaries. Under the application of external electric field, the charge carriers can easily migrate the grains but are accumulated at the grain boundaries. This process can produce large polarization and high dielectric constant. The small conductivity of grain boundary contributes to the high value of dielectric constant at low frequency. The higher value of dielectric constant can also be explained on the basis of interfacial/space charge polarization due to inhomogeneous dielectric structure. The inhomogeneities present in the system may be porosity and grain structure. The polarization decreases with the increase in frequency and then reaches a constant value due to the fact that beyond a certain frequency of external field the hopping between different metal ions (Sn^{4+}, Sn^{2+}, Ni^{2+}) cannot follow the alternating field. It has also been observed that the value of dielectric constant decreases with the increase in Ni dopant. It may be due to the small dielectric polarizability of
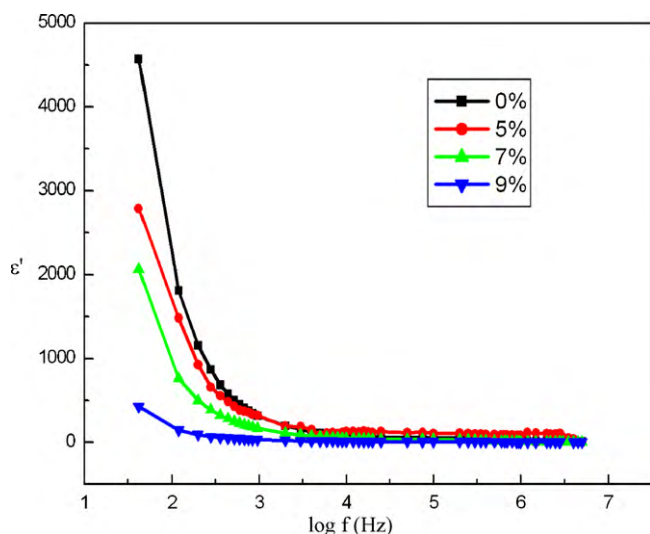
nickel ions ($1.23\,\text{Å}^3$) compared to tin ($2.83\,\text{Å}^3$) [28]. Hence, as the dopant concentration increases more tin ions will be substituted by nickel ions and thereby decreasing the dielectric polarization, which in turn decreases the dielectric constant.

Loss tangent or loss factor $\tan\delta$ represents the energy dissipation in the dielectric system. Fig. 6 shows the variation of dielectric loss factor with frequency at room temperature. It has been observed that $\tan\delta$ decreases with the increase in frequency for all the compositions, which may be due to the space charge polarization. It can also be seen that $\tan\delta$ decreases with the increase in dopant concentration and none of the samples show the loss peak. The peaking behaviour occurs when the hopping (jumping) frequency of metal ions is equal to the frequency of applied ac field.

3.3. Electrical properties

Impedance spectroscopy is a frequency response technique popularly used to unravel the complexities involved in electro ceramic materials. The influence of dopant concentration, impurities and second phase precipitation are also usually investigated by this technique. As the solid electrolytes of practical importance are frequently polycrystalline, bulk and grain boundary conductivities are also taken into account and its separation is of special interest [29]. The electrical behaviour of SnO_2 nanoparticles has been studied over a wide range of frequency at room temperature using ac technique of complex impedance spectroscopy. This technique is widely used to separate the real and imaginary components of electrical parameters and hence provides a clear picture of material properties. Impedance data of materials that have capacitive and resistive components, when plotted in a complex plane plot, appear in the form of a succession of semicircles representing electrical phenomenon due to bulk (grain) material, grain boundary and interfacial phenomenon if any. Generally, the grains are effective in high frequency region while the grain boundaries are effective in low frequency region. Thus the semicircle appearing in the high frequency region corresponds to grain contribution while in low frequency region corresponds to the grain boundary contribution [30]. The electrical properties are often presented in terms of impedance (Z), admittance (Y), permittivity (ε), and electrical modulus (M). The frequency dependent dielectric properties of the materials can be described in terms of complex dielectric constant (ε^*), complex impedance (Z^*), electric modulus (M^*), and dielectric
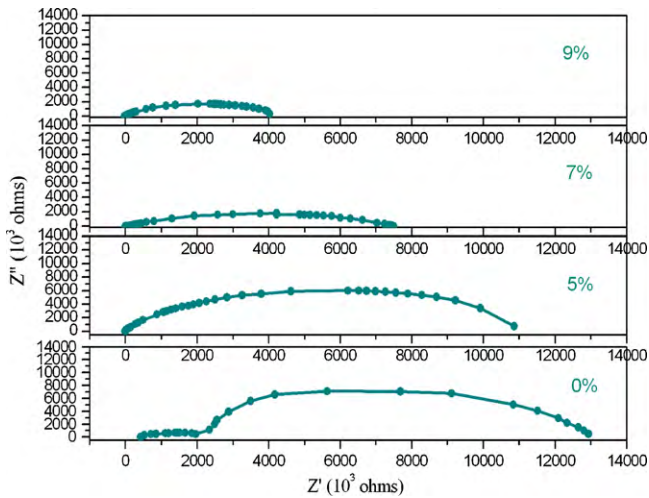

Fig. 5. Variation of real dielectric constant with frequency.

Fig. 7. Nyquist plots for different compositions.

loss ($\tan\delta$). They are related to each other as follows:

$$Z_* = Z' - iZ'' = R - \frac{1}{j\omega C}$$

$$Y_* = Y' - iY'' = j\omega\varepsilon_0\varepsilon_*$$

$$M_* = M' - iM'' = j\omega\varepsilon_0 Z_*$$

and

$$\tan\delta = \frac{\varepsilon''}{\varepsilon'}$$

where $\omega = 2\pi f$ is the angular frequency, R and C are the resistance and capacitance respectively.

The electrical characteristic of a material is exhibited by the appearance of semicircular arcs in Nyquist plots. Fig. 7 shows the complex impedance plots (Nyquist plots) of pure and Ni-doped SnO$_2$ nanoparticles. It can be seen from Fig. 7 there exist two semicircular arcs for pure SnO$_2$, while in case of Ni-doped SnO$_2$ only single semicircle is obtained for all the concentrations of doping. This can be explained on the basis of reduction in grain size with doping. Nanomaterials consist of nanometer size grains which introduce more grain boundaries within the samples. In pure SnO$_2$, the small semicircle obtained in the high frequency region
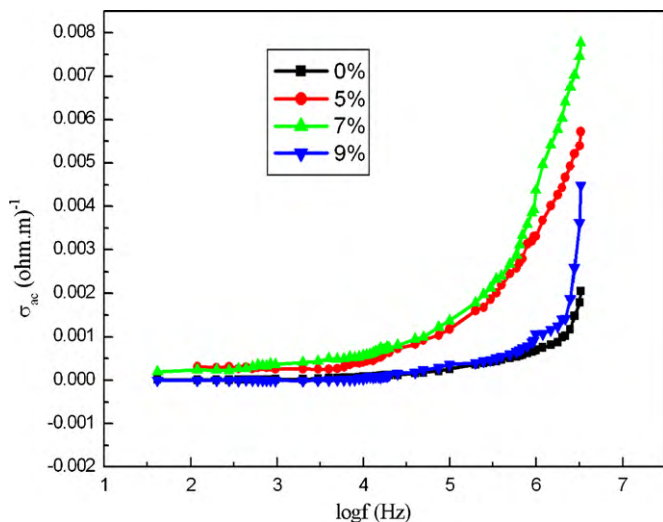

Fig. 8. Variation of ac conductivity with frequency for different compositions.
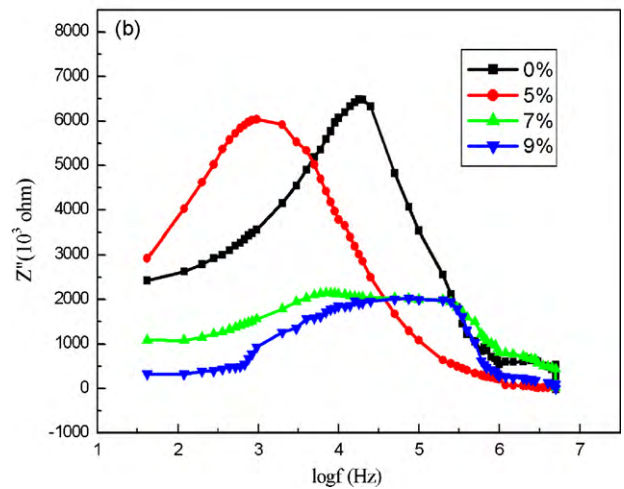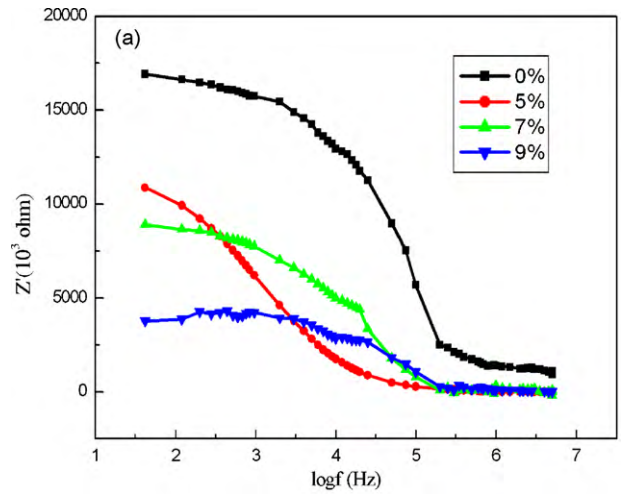

Fig. 9. (a) Variation of real impedance with frequency and (b) variation of imaginary impedance with frequency.

is attributed to the grain conduction while the large semicircle obtained in the low frequency region is due to the grain boundaries as mentioned above. As the particle size decreases the number of grain boundaries increases. Since the grain size of all the three Ni-doped SnO$_2$ nanoparticles is very small, more grain boundaries are introduced in these samples. Fig. 4 clearly shows the development of grain boundaries in doped sample. Hence, the grain boundary effect becomes more dominant over grain contribution and therefore giving one semicircular arc in the Nyquist plot. Moreover, it can be seen from Fig. 7 that total impedance decreases with doping. It is well corroborated from conductivity measurements. It can be seen from Fig. 8 that conductivity increases with doping and it is minimum for pure SnO$_2$, the reason of which is discussed in the next section. Since impedance is inversely proportional to the conductivity, it decreases with the increase in doping.

Fig. 8 shows the variation of electrical conductivity with frequency for different compositions at room temperature. The ac conductivity increases with the increase in frequency for all compositions. Total conductivity of the system is given by

$$\sigma = \sigma_0(T) + \sigma(\omega, T)$$

Here, first term on R.H.S. is dc conductivity which is independent of frequency. The second term is pure ac conductivity due to the electron hopping between the metal ions. It has been observed that ac conductivity gradually increases with the increase in frequency of applied ac field because the increase in frequency enhances the

electron hopping frequency. It can also be seen from Fig. 8 that conductivity increases with the increase in dopant concentration up to 7% and then decreases for 9%. It may be attributed to the fact that the dopants of Ni^{2+} are acceptors for SnO_2 and are usually compensated by the formation of oxygen vacancies. Thus, the increase in dopant concentration increases the oxygen vacancies which results in an increase of free electron density and conductivity. However, the substitution of Sn^{4+} with Ni^{2+} can take place up to a certain limit. When the introduction of Ni^{2+} exceeds this limit, the superfluous Ni^{2+} which cannot substitute Sn^{4+} further will segregate to grain boundary interfaces. Thus, the segregation of Ni^{2+} blocks the building and transportation of electrons and other defects and thereby decreases the conductivity.

Fig. 9(a) shows the variation of real part of impedance (Z') with frequency at room temperature. It is observed that Z' has higher values at lower frequency and decreases with the increase in frequency and attains a constant value in the higher frequency domain for all the compositions. The decrement in the real part of impedance (Z') with the rise in frequency may be due to the increase in ac conductivity with frequency for all the compositions, which is also corroborated by ac conductivity measurements. Fig. 9(b) shows the variation of imaginary part of impedance (Z'') as a function of frequency for different compositions. It is clear from the figure that Z'' shows peaking behaviour and reaches a maximum Z''_{max} and then decrease with further increase in frequency and goes to very small values at higher frequencies. Generally, Debye relaxation peak appears when the frequency of applied electric field matches with the hopping frequency of electrons between the metal ions [26]. The change in the relaxation peak may be due to the change in hopping frequency with doping. It can be seen that the values of Z''_{max} decrease with the increase in doping indicating decrease in loss in the system.

4. Conclusions

We have successfully synthesized Ni-doped SnO_2 nanoparticles using sol–gel method. The XRD patterns exhibit the rutile structure of all the samples. No impurity phase has been observed in XRD. The crystallinity, particle size and lattice constant have been found to decrease with the increase in nickel concentration. The data revealed that the dielectric constant and $\tan\delta$ exhibit the normal dielectric behaviour and decrease with the increase in frequency and dopant concentration, which has been explained in the light of Maxwell–Wagner model. The ac conductivity shows the frequency and composition dependent behaviour. It increases with the increase in frequency and dopant concentration. Complex impedance spectra show two semicircles corresponding to pure SnO_2 nanoparticles while one semicircle for Ni-doped samples, suggesting the dominance of grain boundary resistance in the doped samples.

References

[1] P.G. Li, X. Guo, X.F. Wang, W.H. Tang, J. Alloys Compd. 479 (2009) 74–77.
[2] C. Wang, J. Li, Y. Zhang, Y. Wei, J. Liu, J. Alloys Compd. 493 (2010) 64–69.
[3] M. Batzill, U. Diebold, Prog. Surf. Sci. 79 (2005) 47–154.
[4] C. Kilic, A. Zunger, Phys. Rev. Lett. 88 (2002) 095501.
[5] L.M. Fang, X.T. Zu, Z.J. Li, S. Zhu, C.M. Liu, W.L. Zhou, L.M. Wang, J. Alloys Compd. 454 (2008) 261–267.
[6] A.S. Albuquerque, J.D. Ardisson, W.A.A. Macedo, T.S. Plivelic, I.L. Torriani, J. Larrea, E.B. Saitovitch, J. Magn. Magn. Mater. 272–276 (2004) 2211–2213.
[7] M. Huh, S. Kim, J. Ahn, J. Park, B. Kim, Nanostruct. Mater. 11 (1999) 211.
[8] J. Zhang, L. Gao, J. Solid State Chem. 177 (2004) 1425–1430.
[9] Y. Liu, F. Yang, X. Yang, Colloids Surf. A 312 (2008) 219–225.
[10] J. Pena, J. Perez-Pariente, M. Vallet-Regi, J. Mater. Chem. 13 (2003) 2290–2296.
[11] L. Fraigi, D.G. Lamas, N.E.W. Reca, Nanostruct. Mater. 11 (1999) 311–318.
[12] D. Davazoglou, Thin Solid Films 302 (1997) 204–213.
[13] R.G. Gordan, MRS Bull. 25 (2000) 52.
[14] E.T.H. Tan, G.W. Ho, A.S.W. Wong, S. Kawi, A.T.S. Wee, Nanotechnology 19 (2008) 255706.
[15] K. Jain, R.P. Pant, S.T. Lakshmikumar, Sens. Actuators B 113 (2006) 823–829.
[16] J.A. Aguiler Martinez, M.B. Hernandez, A.B. Glot, M.I. Pech-Canul, J. Phys. D: Appl. Phys. 40 (2007) 7097–7102.
[17] A.A. Yadav, E.U. Masumdar, A.V. Moholkar, M. Neumann-Spallart, K.Y. Rajpure, C.H. Bhosale, J. Alloys Compd. 488 (2009) 350–355.
[18] J. Joseph, V. Mathew, K.E. Abraham, Chin. J. Phys. 45 (2007) 84–97.
[19] A.V. Gaponov, A.B. Glot, J. Mater. Sci.: Mater. Electron. 21 (2010) 331–337.
[20] A.L. Patterson, Phys. Rev. Online Arch. (Prola) 56 (1939) 978–982.
[21] H. Yang, W. Jin, L. Wang, Mater. Lett. 57 (2003) 3686–3689.
[22] M. Hirano, K. Ota, H. Iwata, Chem. Mater. 16 (2004) 3725–3732.
[23] X. Fu, H. Zhang, S. Niu, Q. Xin, J. Solid State Chem. 178 (2005) 603–607.
[24] D.R. Leite, W.C. Las, G. Brankovic, M.A. Zaghete, M. Cilence, J.A. Varela, Mater. Sci. Forum 498–499 (2005) 337–341.
[25] J.A. Cerri, E.R. Leite, D. Gouvea, E. Longo, J. Am. Ceram. Soc. 79 (1996) 799–804.
[26] A.M. Abdeen, O.M. Hemeda, E.E. Assem, M.M. El-Sehly, J. Magn. Magn. Mater. 238 (2002) 75.
[27] T. Prodromakis, C. Papavassiliou, Appl. Surf. Sci. 255 (2009) 6989–6994.
[28] R.D. Shannon, J. Appl. Phys. 73 (1993) 348–366.
[29] P.R. Bueno, J.A. Varela, E. Longo, J. Eur. Ceram. Soc. 27 (2007) 4313–4320.
[30] A.K. Baral, V. Sankaranarayanan, Appl. Phys. A 98 (2010) 367–373.